Available online at www.sciencedirect.com

ScienceDirect

Procedia CIRP 23 (2014) 110 – 115

www.elsevier.com/locate/procedia

Conference on Assembly Technologies and Systems

Robotic assembly of aircraft engine components using a closed-loop alignment process

Lars Tingelstad[a,*], Olav Egeland[a]

[a]*Department of Production and Quality Engineering, Norwegian University of Science and Technology, S.P. Andersens vei 5, Trondheim 7465, Norway*

* Lars Tingelstad. Tel.: +47-7359-3800; fax: +47-7359-7117. *E-mail address:* lars.tingelstad@ntnu.no

Abstract

This paper presents robotic assembly of aircraft engine components that cannot be assembled using traditional robotic assembly methods. The reason for this is uncertainty in shape and dimensional accuracy due to imperfections in the preceding manufacturing processes. In addition, the aircraft engine components are designed as complex geometry thin shell parts that are compliant in certain directions, resulting in assemblies which cannot meet manufacturing tolerances without forcing the components into shape and position. We present a solution to the problem using two real-time controlled industrial robots and a high accuracy laser triangulation sensor in a closed loop alignment process.

Selection and peer-review under responsibility of the International Scientific Committee of 5th CATS 2014 in the person of the Conference Chair Prof. Dr. Matthias Putz matthias.putz@iwu.fraunhofer.de

Keywords: 3D-Image processing; Adaptive manufacturing; Assembly; Control; Robot; Sensor; Servo system

1. Introduction

Robotic assembly of aerospace structures is a challenging task as the components tend to be large and of light weight, and there are strict tolerances. As the production batches are relatively small, the drive for robotic automation has not been as strong as in e.g. the automotive industry. Robotic solutions for preprogrammed drilling, riveting, assembly, painting and inspection are currently commercially available for the production of aerospace systems. Still there are unsolved robotic tasks in aerospace production that will require a larger extent of sensor feedback for adjustments due to uncertainties and inaccuracies. Such sensor-based control systems for robots are becoming feasible due to the recent developments in industrial robot control systems [1,2], and the strong development in robot control systems in research labs [3,4]. This makes it possible to implement new and advanced solutions for robotic solutions in aerospace assembly operations.

Robot force-control is a well-established technique [5] which have been used for advanced applications in aerospace production. This includes robotic drilling with force feedback where the objective is to clamp the tool to eliminate sliding and deformations effects while drilling [6], and force control for robotic drilling and riveting where the two parts are compressed together with more than 1000 N to achieve stable drilling [7].

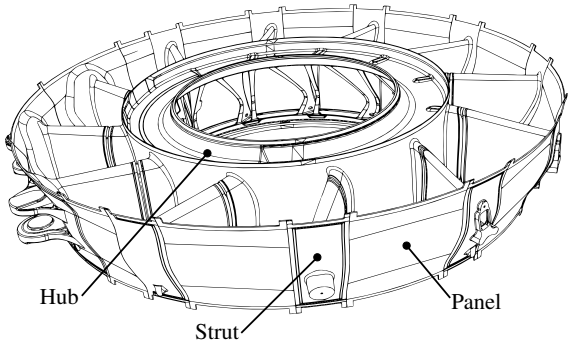

Fig. 1: GEnx Turbine Rear Frame.

Robotic force control for the assembly of a flexible aircraft structure was reported in [8] where force control was used in the constraint-based task specification framework of [9] for alignment of a semi-compliant rib with multiple surfaces.

In addition, non-contact sensors have been used for the correction of preprogrammed robot assembly operations. A system for robotic assembly of fabricated aero-engine components is presented in [10]. The system is based on a combination of non-contact metrology systems and mathematical models

Selection and peer-review under responsibility of the International Scientific Committee of 5th CATS 2014 in the person of the Conference Chair Prof. Dr. Matthias Putz matthias.putz@iwu.fraunhofer.de
doi:10.1016/j.procir.2014.10.070

which makes it possible to compensate for deformation in the fabricated components, thereby reducing the reliance on fixturing, and ensuring flexibility and re-configurability of the system. The authors point out that the automated assembly of aero-engine structures has been limited so far due to the variability of the components as a result of previous manufacturing processes, and that improved sensor systems are needed to compensate for deformation and misalignment of mating parts. The paper [10] also cites other works on robotic applications in the aerospace industry where there is significant interest in adopting external metrology systems to improve the capability of the robotic systems.

Assembly operations with non-rigid components that need correction to meet assembly tolerances can be characterized as compliant assemblies [11,12]. A sense-act method is described in [11] where the aim is to reduce the variation in compliant assembly. In this method each component is positioned and fixed in its nominal position. Then the components are measured and the dimensional problem is decomposed into a rigid-body displacement and a compliant deformation from the nominal shape. The required tooling adjustment is then applied to the extent that it is feasible given the tooling constraints and the components to be assembled. It is noted by the authors that the tooling adjustment algorithm depends on accurate determination on the required adjustment to minimize the total deviation of the assembly. An improvement to this can be achieved with feedback control, which is the method we propose in the present paper.

This paper presents a robotic system for assembly of aircraft engine components using a closed-loop alignment process based on the use of laser triangulation. The engine part that is studied is the Turbine Rear Frame (TRF) of the General Electric GEnx aircraft engine series, as shown in Fig. 1. The TRF is mounted after the turbine and contains engine mounts and bearings for the rotating low pressure shaft [13]. The TRF is assembled from three types of components that are thin shell cast and cold-forged. These components have complex geometry, and does not have the required accuracy in shape and dimension for robotic assembly with pre-programmed motions. This is due to effects like shrinkage in the casting process and springback effects in the cold-forging process. However, the deviation in accuracy can be compensated for during assembly as the parts are typically compliant in the directions where the inaccuracy is found. This means that the TRF can be assembled with the required accuracy by forcing the components into the correct shape. So far this has been done manually with complex fixtures before the assembly is tack welded in the correct shape, which is done in preparation for the seam welding. These manual operations are time-consuming and costly, which motivates the current study on how to do this automatically with robotic operation.

An advantage of this method is that the assembly process does not dependent on an accurate model of the deformation of the components. Instead of calculating an adjustment in an open-loop sense-act process, a feedback approach is used. The alignment process presented is implemented by measuring the offset between two TRF components using a high accuracy laser triangulation sensor, while one of the robots is in contact with one of the components to manipulate its shape. The robot system is shown in Fig. 2. The resulting system makes it possible to assemble the components well within the defined manufacturing tolerances.

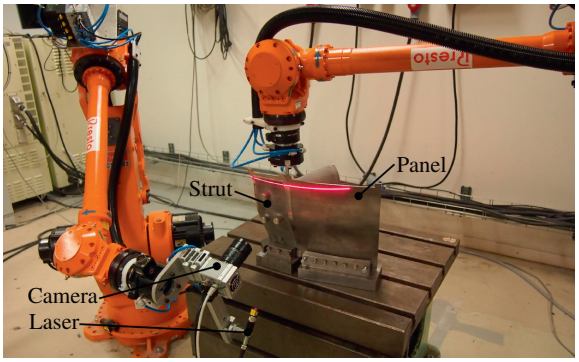

Fig. 2: System setup. The alignment robot is in contact with the panel, manipulating its shape by pushing or pulling on one of the upper corners.

A previous version of the system was presented in [14]. The previous test cell had two robots and a high-precision laser distance sensor mounted on one of the robots. The offset between the components was found with the laser distance sensor, and the offset was corrected in a sense-act process, which was repeated until the offset distance was within a certain tolerance. The present solution leads to a faster adjustment cycle due to the feedback control solution.

The paper is organized as follows. Section 2 presents the equipment used and the developed system in detail. Section 3 presents the experimental results. Section 4 concludes the paper and presents further work.

2. System overview

The hardware of the presented system consists of two industrial robots, a laser-triangulation sensor and a fixture. The physical setup is shown in Fig. 2. The following sections presents the system in detail.

2.1. Industrial Robots

The industrial robots used in the system are Nachi Fujikoshi SC15F-2 robots equipped with AX-series robot controllers. An Olimex SAM9-L9260 single board computer (SBC) is installed between the high and low level controller. The SBC intercepts the communication and provides a position control interface over UDP, with a control frequency of 100 Hz.

2.2. Laser Triangulation Sensor

The laser triangulation sensor system was mounted on one of the two robots used in the experiment. The laser line module was a ZLaser 100 mW laser with a wavelength of 660 nm and a cylindrical lens with a fan angle of 45°. The camera was a Automation Technology C4-2040-GigE camera with a GeniCam interface. The laser line peak positions are evaluated and converted into high resolution (1/64 pixel) height profiles on board the camera. The camera is equipped with 90 dB dynamic range with the possibility of performing High Dynamic Range imaging, which makes it possible to measure on difficult areas of the

TRF components. The maximum profile output speed is 340 Hz with a full frame image of 2048x1088 pixels, which can be increased with a smaller region of interest. The camera is set up to also output the corresponding intensity data.

2.2.1. Camera and laser calibration

The intrinsic parameters of the camera was calibrated using the Camera Calibration Toolbox for MATLAB [15]. The system was implemented using the OpenCV library [16].

The extrinsic parameters of the camera was found using a 3-plane calibration object of known dimensions and an implementation based on the method presented in [17]. The calibration method estimates the homography matrices $\boldsymbol{H}_{i=1,2,3}$ between the image plane and the three planes on the calibration object. These matrices combined with the known plane heights maps points in the normalized image plane, $\boldsymbol{x}_i = (x_i, y_i)$, to the corresponding 3D points, $\boldsymbol{P}_i = (X_i, Y_i, Z_i)$, on the calibration object. The laser plane, which is given in terms of a point $\boldsymbol{P}_0$ belonging to the plane and a normal vector $\boldsymbol{n}$, was then found by projecting the laser line on the calibration object, recording the normalized image plane coordinates and calculating the 3D points of the laser line onto the calibration object. Then the parameters of the plane were found from the 3D points of the plane using orthogonal distance regression and singular value decomposition using the following equations:

$$\begin{aligned} \boldsymbol{P}_i &= (X_i, Y_i, Z_i) \\ \boldsymbol{P}_0 &= \frac{1}{N}\sum_{i=1}^{N} \boldsymbol{P}_i \\ \boldsymbol{A} &= (\boldsymbol{P}_1 - \boldsymbol{P}_0, \ldots, \boldsymbol{P}_N - \boldsymbol{P}_0)^T \\ \boldsymbol{A} &= \boldsymbol{U}\boldsymbol{S}\boldsymbol{V}^T. \end{aligned}$$

Finally, the normal of the plane $\boldsymbol{n}$ is found as the last column of $\boldsymbol{V}$.

2.2.2. 3D reconstruction using laser and camera

The 3D coordinates of the laser line are reconstructed from the normalized image coordinates. Let $\boldsymbol{P}_c$ be the position of the camera center expressed in the object frame, then $(\boldsymbol{P}_0 - \boldsymbol{P}_c) \cdot \boldsymbol{n}$ is the distance from the laser plane to the camera center. Let $\boldsymbol{l}$ be the unit vector from the camera center to a point on the laser line. Then the distance ρ from the camera center to the point $\boldsymbol{P}$ on the laser line is given by

$$\begin{aligned} \rho &= \frac{(\boldsymbol{P}_0 - \boldsymbol{P}_c) \cdot \boldsymbol{n}}{\boldsymbol{l} \cdot \boldsymbol{n}} \\ \boldsymbol{P} &= \rho \boldsymbol{l} + \boldsymbol{P}_c, \end{aligned} \tag{1}$$

where $\boldsymbol{P}$ is given in object coordinates.

2.3. Trajectory Generation

The trajectory generator used in the system is a operational space velocity generator. A 6-DOF twist vector, expressed in the base frame is computed in each control cycle and the corresponding motion is executed by the robot system until a configurable timeout. The timeout used in the system is 0.01 s, corresponding to the control frequency of the robots.

Real-time trajectory generation was performed using the PyMoCo software package [18]. PyMoCo is a software package for external real-time trajectory generation for industrial robots, and is entirely implemented in Python. The framework is suited for applications with a control frequency up to 100 Hz, computational deadlines no shorter than some milliseconds and jitter tolerance at the order of a millisecond.

2.4. Offset Measurement

The offset measurement consists of two main steps: 1) Weld seam detection. 2) Offset computation.

2.4.1. Weld Seam Detection

The weld seam detection is based on finding the same edge in the laser line position data and the corresponding intensity data. The implemented algorithm are based on standard edge detection techniques: Filtering, calculation of derivative, extrema detection and thresholding.

The image coordinates (u, v) are given in pixels. The camera is aligned with the laser so that the laser line is nominally in the u direction. The offset between the two aircraft engine components is computed from the position $v = v(u)$ of the laser line. The intensity of the laser line is denoted $I = I(u)$. The laser line peak positions and the corresponding intensity data are both one-dimensional arrays. The weld seam position is denoted u_w.

Filtering. The laser line peak positions v had a very high signal to noise (SNR) ratio, and was filtered using a median filter to remove any shot noise from the signal. A median filter was selected as it is often referred to as having better properties than linear filters for removing noise in the presence of edges [19]. The median filtering was performed using a kernel size of 3. The filtered laser line peak positions is shown in Fig. 3a. The filtered laser line peak position signal is denoted v^* in the following sections.

The corresponding intensity data I had a lower SNR than v and was filtered using a median filter with a kernel size of 15. The resulting intensity signal is shown in Fig. 3b. The filtered laser line intensity signal is denoted I^* in the following sections.

Find Derivative. The first derivative of v^* was found by convoluting v^* with the differentiation kernel $D_x = \begin{bmatrix} -1 & 0 & 1 \end{bmatrix}$,

$$\frac{\partial}{\partial u} v^* = v^*_u = D_u * v^*.$$

This method was selected due to the low SNR, as well as resulting in large magnitude peaks ensuring robust peak detection in the next stage of the weld seam detection.

Convolution of the median filtered I^* using just the differentiation kernel performed badly, due to the presence of Gaussian noise in the signal [19]. The 1st order Gaussian derivative kernel, $G_{\sigma,x}$, was selected instead due to its signal smoothing

properties.

$$G_{\sigma,x} = \frac{1}{\sqrt{2\pi}\sigma} \exp\left(\frac{-x^2}{2\sigma^2}\right)$$
$$\frac{\partial}{\partial x} I^* = I^*_x = (D_x * G_{\sigma,x}) * I^*.$$

A kernel with a standard deviation of $\sigma = 3.0$ was used in the experiments. A sudden drop in the intensity at the weld seam position is seen in Fig. 3b. This drop in intensity resulted in a large magnitude peak ensuring a stable weld seam detection even when the offset between the two components was very small, resulting in small to non-existent peaks in v^*_u. Correct weld seam position detection is critical as the robot is in contact with the components and an erroneous movement may lead to component and equipment failure.

Find Extremas and Threshold. The maximum and minimum of the first derivative of the signals were found by iterating through the signals looking for values which were surrounded by lower or larger values. A look ahead from the peak candidate was used to distinguish between actual peaks and signal jitter. A threshold value specified the minimum difference between a peak and the following points.

2.4.2. Offset Computation

Once the weld seam position u_w was found, using the algorithm in the previous section, we were able to find the physical offset δ using the difference in v^* on each side of the weld seam.

First a 1st degree polynomial $p_\mathrm{l}(u_j) = a_1 u_j + a_0$ was fitted to the data points to the left of the weld seam. This was done using a least squares fit minimizing the error

$$E = \sum_{j=u_\mathrm{w}+u_\mathrm{start}}^{u_\mathrm{w}+u_\mathrm{stop}} |p(u_j) - v^*(u_j)|^2$$

Here u_start and u_stop were chosen so that the polynomial was fitted to a smooth segment of the signal, and to reduce possible noise at the weld seam area due to reflection on the edges of the components. The same procedure was then performed on the data points to the right of the weld seam, resulting in the polynomial $p_\mathrm{r}(u_j)$.

The two acquired polynomials were then used to calculate the physical offset δ between the two aircraft engine components by evaluating p_l and p_r at the weld seam u_w and using these points as input to Eqn. (1) resulting in $\boldsymbol{P}_\mathrm{l}$ and $\boldsymbol{P}_\mathrm{r}$.

$$\delta = \|\boldsymbol{P}_\mathrm{r} - \boldsymbol{P}_\mathrm{l}\|$$

2.5. Alignment Correction Controller

As explained in the introduction, previous solutions have been implemented with a sense-act solution where alignment errors have been measured, then a correction has been done based on a calculated increment computed from a model [10],

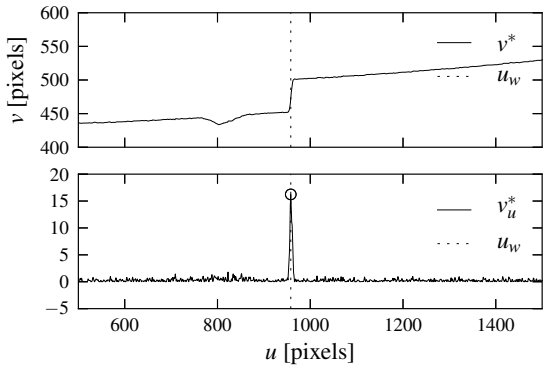

(a) Full frame image with laser line before adjustment, with the maximum in the first derivative found at $u_\mathrm{w} = 958$.

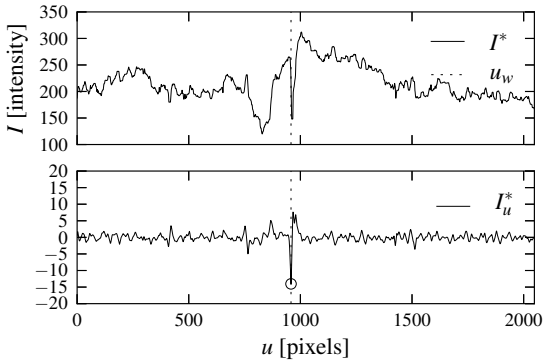

(b) Corresponding intensity data of laser line with the minimum in the first derivative found at $u_\mathrm{w} = 958$.

Fig. 3: Weld seam detection

or with an increment using a fixed step size [14]. This is typically done iteratively where a new measurement has been made after the correction is completed, and new corrections are made until the required accuracy is achieved. This will be time-consuming and may lead to excessive stress on the structure.

We therefore propose a new solution where we use continuous feedback from the alignment measurement. This leads to faster execution and better control of the correcting action. It turns out that proportional feedback control is well suited for the problem. The output of the proportional controller is the operational space velocity $\dot{\boldsymbol{x}}_d$, so that

$$\dot{\boldsymbol{x}}_d = \begin{bmatrix} \upsilon_x & \upsilon_y & \upsilon_z & \omega_x & \omega_y & \omega_z \end{bmatrix}^T$$
$$= \begin{bmatrix} \upsilon_x & 0 & 0 & 0 & 0 & 0 \end{bmatrix}^T,$$

where the physical configuration of the system is so that the alignment direction is in the x direction of the base frame of the alignment robot. The proportional controller is given by:

$$\upsilon_x = K_p \delta_e = -K_p(\delta - \delta_d), \quad (2)$$

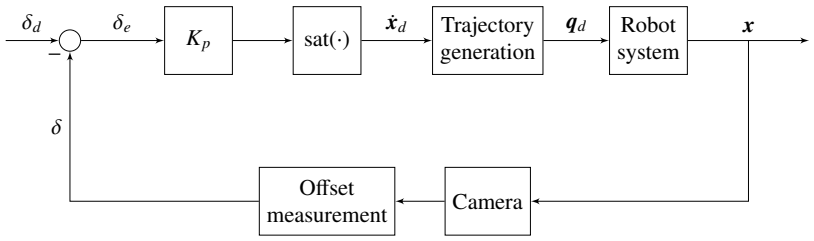

Fig. 4: The block diagram of the feedback controller shows the proportional feedback controller with feedback from the alignment error δ_e which is measured with a camera. The control variable is saturated with the sat(·) function to limit the commanded velocity $\dot{\boldsymbol{x}}_d$.

where υ_x is the commanded correction velocity in the x direction.

One modification of the feedback controller is required to avoid excessive velocity in the correcting motion. This is done with a saturation on the velocity υ_x generated by the feedback control. The resulting controller is:

$$\mathrm{sat}(\upsilon_x) = \begin{cases} \upsilon_{\max} & \text{if } \delta_e > \delta_{\mathrm{thrs}} \\ K_p\delta_e & \text{if } -\delta_{\mathrm{thrs}} \le \delta_e \le \delta_{\mathrm{thrs}} \\ -\upsilon_{\max} & \text{if } \delta_e < -\delta_{\mathrm{thrs}} \end{cases},$$

where the parameters of the saturation function are related by the equation

$$\upsilon_{\max} = K_p\delta_{\mathrm{thrs}} \tag{3}$$

The desired offset δ_d was based on the manufacturing tolerances of the assembly. This controller gives fast and stable alignment, and will not exceed the physical limits of the alignment robot or the components.

A block diagram of the alignment correction controller is shown in Fig. 4.

The trajectory generator was, as mentioned, a operational space velocity controller. The controller was based on an Jacobian inverse control scheme which computed the desired joint position vector $\boldsymbol{q}_d$. The robot executes the motion resulting in a change in the current robot position $\boldsymbol{x}$, and thus also a change in the physical offset δ between the components.

3. Experimental results

A series of experiments were performed to verify the capability of the developed system.

Good results were obtained with the feedback controller when the maximum correction velocity $\upsilon_{\max}$ was set to 1 mm/s, which was found to be a good compromise between speed of execution and the need for limiting the risk for collisions and high stress on the structure. The feedback gain was selected to be $K_p = 1$, which gave a exponential convergence of the alignment error with a time constant of 1 second. The resulting threshold value was then found from Eqn. (3) to be 1 mm.

The results from the weld seam detection method for one of the experiments are shown in Fig. 3. It is seen that the weld seam was successfully located from the laser line peak position data v^* and the corresponding intensity data I^*. The weld seam was found at $u_{\mathrm{w}} = 958$ in both signals.

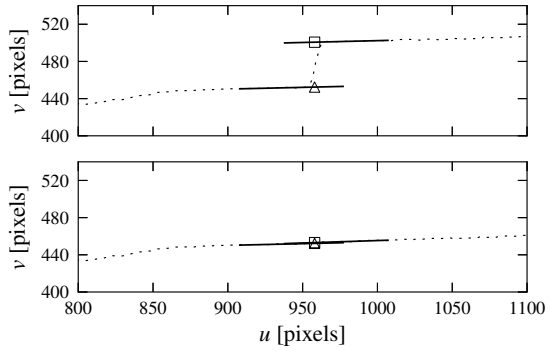

Fig. 5: The upper curve shows an enlarged detail of Fig. 3a showing the jump in the laser line position signal v^* due to the misalignment before the correction. The lower curve shows the same enlarged detail after the correction has been completed. The error in alignment was compensated from an initial error of $\delta_{\mathrm{start}} = 6.94$ mm to a final error of $\delta_{\mathrm{stop}} = 0.12$ mm, which is well within the manufacturing tolerance.

The results from the offset computation are shown in Fig. 5. The parameters of the polynomial fitting were set to $u_{\mathrm{start}} = -75$ and $u_{\mathrm{stop}} = 5$ for the polynomial fit to the left of the weld seam, and $u_{\mathrm{start}} = 5$ and $u_{\mathrm{stop}} = 125$ for the right side of the weld seam. The limits are not symmetrical due to physical differences on the two components to be aligned, as seen in Fig. 3a. The offset computation proved to be stable during the whole alignment process in all experiments.

Fig. 6 shows the plot of the output of the proportional controller as well as the corresponding operational space velocity. The initial offset was $\delta_{\mathrm{start}} = 6.94$ mm. The final offset after alignment was $\delta_{\mathrm{stop}} = 0.12$ mm The parameters $\upsilon_{\max}$ and δ_{thrs} were selected so that the transition from maximum to proportional velocity was as smooth as possible.

The precision of the final alignment are a direct result of the resolution of the camera and the control resolution of the robot.

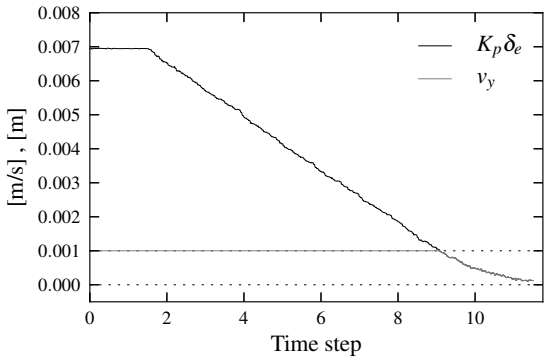

Fig. 6: Output of the proportional controller and corresponding operational space velocity υ_x. In this experiment the feedback gain was selected to be $K_p = 1$, the maximum velocity was set to $\upsilon_{\max} = 0.001$ mm/s, and the offset threshold was set to $\delta_{\text{thrs}} = 0.001$ mm.

4. Conclusions and further work

A system for closed-loop alignment of complex geometry aircraft engine components has been presented. The system has been experimentally validated and is able to align two components in a closed-loop compliant alignment process with an accuracy of 0.12 mm using a laser triangulation sensor and a real-time controlled industrial robot. The system was shown to be capable of aligning the components well within manufacturing tolerances.

Further work will include global analysis of the weld seam alignment process using in-process 3D-scans of the components and the weld seam, resulting in optimal placement and alignment offset of each area to be welded. The work will also be extended to include force control.

Acknowledgements

This work was partly funded by the EU 7FP project IFaCOM (Intelligent Fault Correction and self Optimizing Manufacturing Systems FoF NMP - 285489).

References

[1] Hirzinger, G., Bals, J., Otter, M., Stelter, J.. The DLR-KUKA success story: Robotics Research Improves Industrial Robots. Robotics Automation Magazine, IEEE 2005;12(3):16–23. doi:10.1109/MRA.2005.1511865.

[2] Brogårdh, T.. Present and future robot control development -An industrial perspective. Annual Reviews in Control 2007;31(1):69 – 79. URL: http://www.sciencedirect.com/science/article/pii/S1367578807000077. doi:http://dx.doi.org/10.1016/j.arcontrol.2007.01.002.

[3] Bruyninckx, H.. Open robot control software: the OROCOS project. In: IEEE Int. Conf. Robotics and Automation. 2001, p. 2523–2528.

[4] Kubus, D., Nilsson, K., Johansson, R., editors. ICRA 2010 Workshop on Innovative Robot Control Architectures for Demanding (Research) Applications. 2010. URL: http://www.rob.cs.tu-bs.de/en/news/icra2010.

[5] Siciliano, B., Sciavicco, L., Villani, L., Oriolo, G.. Force control. In: Robotics. Advanced Textbooks in Control and Signal Processing; Springer London. ISBN 978-1-84628-641-4; 2009, p. 363–405. URL: http://dx.doi.org/10.1007/978-1-84628-642-1_9. doi:10.1007/978-1-84628-642-1_9.

[6] Olsson, T., Haage, M., Kihlman, H., Johansson, R., Nilsson, K., Robertsson, A., et al. Cost-efficient drilling using industrial robots with high-bandwidth force feedback. Robotics and Computer-Integrated Manufacturing 2010;26(1):24 – 38. URL: http://www.sciencedirect.com/science/article/pii/S0736584509000039. doi:http://dx.doi.org/10.1016/j.rcim.2009.01.002.

[7] Degoulange, E., Dauchez, P., Pierrot, F., Prat, P.. Determination of a reference model for controlling the deformation of an industrial robot. application to riveting in aeronautics. In: Intelligent Robots and Systems '94. 'Advanced Robotic Systems and the Real World', IROS '94. Proceedings of the IEEE/RSJ/GI International Conference on; vol. 1. 1994, p. 343–351 vol.1. doi:10.1109/IROS.1994.407371.

[8] Stolt, A., Linderoth, M., Robertsson, A., Jonsson, M., Murray, T.. Force controlled assembly of flexible aircraft structure. In: Robotics and Automation (ICRA), 2011 IEEE International Conference on. 2011, p. 6027–6032. doi:10.1109/ICRA.2011.5979962.

[9] Schutter, J.D., Laet, T.D., Rutgeerts, J., Decr, W., Smits, R., Aertbelin, E., et al. Constraint-based task specification and estimation for sensor-based robot systems in the presence of geometric uncertainty. The International Journal of Robotics Research 2007;26:433–455.

[10] Jayaweera, N., Webb, P., Johnson, C.. Measurement assisted robotic assembly of fabricated aero-engine components. Assembly Automation 2010;30(1):56–65.

[11] Hu, S.J., Camelio, J.. Modeling and Control of Compliant Assembly Systems. CIRP Annals - Manufacturing Technology 2006;55(1):19–22. doi:10.1016/S0007-8506(07)60357-6.

[12] Merkley, K.G.. Tolerance analysis of compliant assemblies. Ph.D. thesis; Brigham Young University; 1998.

[13] Ericsson, A., Rundström, F.. Optimisation of low cycle fatigue life in jet engine frame. Master's thesis; Linköping University; 2006. URL: http://www.solid.iei.liu.se/Publications/Master_thesis/2007/Albert_Eriksson.pdf.

[14] Tingelstad, L., Capellan, A., Thomessen, T., Lien, T.K.. Multi-Robot Assembly of High-Performance Aerospace Components. In: IFAC Symposium on Robot Control (SYROCO), 10th International. 2012,.

[15] Bouguet, J.Y.. Camera calibration toolbox for Matlab. 2013. URL: http://www.vision.caltech.edu/bouguetj/calib_doc/.

[16] Bradski, G.. The OpenCV Library. Dr Dobb's Journal of Software Tools 2000;.

[17] Fauster, E., Schalk, P., Tratnig, M.. Calibration Method for Light Sectioning Measurement Systems. In: 2nd WSEAS International Conference on Signal, Speech and Image Processing (ICOSSIP 2002). 2002, p. 1891–1898.

[18] Lind, M., Tingelstad, L., Schrimpf, J.. Real-time robot trajectory generation with python. In: Workshop on Robot Motion Planning: Online, Reactive and in Real-Time. 2012 IEEE/RSJ International Conference on Intelligent Robots and Systems, IROS 2012, Vilamoura, Algarve, Portugal, October 7-12. 2012,URL: http://www.reflexxes.com/iros2012ws/Paper_19.pdf.

[19] Szeliski, R.. Computer vision algorithms and applications. 2011. URL: http://dx.doi.org/10.1007/978-1-84882-935-0.